

The *XMM-Newton* spectra of the 2012 outburst of the black-hole candidate 4U 1630–47 revisited

Yanan Wang^{1*}, Mariano Méndez¹

¹*Kapteyn Astronomical Institute, University of Groningen, PO BOX 800, NL-9700 AV Groningen, the Netherlands*

Accepted ? December ?. Received ? December ?; in original form ? December ?

ABSTRACT

Recent *XMM-Newton* observations of the black-hole candidate 4U 1630–47 during the 2012 outburst revealed three relativistically Doppler-shifted emission lines that were interpreted as arising from baryonic matter in the jet of this source. Here we reanalyse those data and find an alternative model that, with less free parameters than the model with Doppler-shifted emission lines, fits the data well. In our model we allow the abundance of S and Fe in the interstellar material along the line of sight to the source to be non solar. Among other things, this significantly impacts the emission predicted by the model at around 7.1 keV, where the edge of neutral Fe appears, and renders the lines unnecessary. The fits to all the 2012 *XMM-Newton* observations of this source require a moderately broad emission line at around 7 keV plus several absorption lines and edges due to highly ionised Fe and Ni, which reveal the presence of a highly-ionised absorber close to the source. Finally, our model also fits well the observations in which the lines were detected when we apply the most recent calibration files, whereas the model with the three Doppler-shifted emission lines does not.

Key words: accretion, accretion disk–binaries: X-rays: individual (4U 1630–47)

1 INTRODUCTION

The soft X-ray transient 4U 1630–47 (Jones et al. 1976; Parmar et al. 1995) shows regular outbursts every 600–690 days (Abe et al. 2005; Tomsick et al. 2014). The source has been classified as a black hole (Parmar et al. 1986) because of the similarity of its spectral and timing properties to those of systems with measured black-hole masses (e.g., Barret et al. 1996; Abe et al. 2005). 4U 1630–47 shows strong absorption by neutral material along the line of sight, with a hydrogen column density $N_{\text{H}} = 5 - 12 \times 10^{22} \text{ cm}^{-2}$ (e.g., Tomsick et al. 1998), and both IR (Augusteijn et al. 2001) and radio emission (Hjellming et al. 1999) were detected during the 1998 outburst of this source. The optical counterpart of 4U 1630–47 has not been identified, mostly due to the high reddening and the location of the source in a crowded star field (Parmar et al. 1986).

Absorption lines due to highly ionised material have been observed in the spectrum of 4U 1630–47 (Kubota et al. 2007; Rózańska et al. 2014; Díaz Trigo et al. 2014; Miller et al. 2015). Using *Suzaku* observations carried out in 2006, Kubota et al. (2007) studied these absorption line features in relation to the accretion-disc parameters, and concluded that the lines were due to a wind. Using the same *Suzaku* data, Rózańska et al. (2014) proposed that the absorption lines could be produced effectively in

the accretion disc atmosphere. Using *XMM-Newton* observations, Díaz Trigo et al. (2014) found a thermally/radiatively driven disc wind in 4U 1636–47; the wind becomes more photoionised as the luminosity of the source increases. Recently, Miller et al. (2015) analyzed *Chandra* observations of 4U 1630–47 and three other galactic black hole candidates. For 4U 1630–47, they found that the wind consists of at least two absorption zones with velocities of -200 km s^{-1} and -2000 km s^{-1} , respectively. They also found that, in some respects, these zones correspond to the broad-line region in active galactic nuclei.

Díaz Trigo et al. (2013) analysed two *XMM-Newton* and two quasi-simultaneous observations with the Australia Telescope Compact Array (ATCA) carried out during the 2012 outburst of 4U 1630–47. Díaz Trigo et al. (2013) found three relatively narrow emission lines in the X-ray spectrum of one of these observations that they identified as arising from baryonic matter in a jet. The three lines had energies of 4.04 keV, 7.28 keV and 8.14 keV, respectively, which Díaz Trigo et al. (2013) interpreted as the red- and blueshifted component of Fe xxvi Ly α and the blueshifted component of Ni xxviii Ly α , respectively. From the radio data, Díaz Trigo et al. (2013) confirmed that there was an optically thin jet in 4U 1630–47 at the time of that observation. Hori et al. (2014) investigated *Suzaku* and Infrared Survey Facility observations of 4U 1630–47 during the same outburst, at a time when the source was in the very high state. These observations were carried out three to five days after the *XMM-Newton*

* E-mail: yanan@astro.rug.nl

observations of Díaz Trigo et al. (2013). The *Suzaku* X-ray spectra, however, did not show the Doppler-shifted emission lines of the jet reported by Díaz Trigo et al. (2013). Using *Chandra* and ATCA observations taken eight months prior to the *XMM-Newton* observations of Díaz Trigo et al. (2013), Neilsen et al. (2014) reported a similar result to that of Hori et al. (2014).

When fitting the *Chandra* data of 4U 1630–47, Neilsen et al. (2014) allowed the abundance of Si, S and Ni in the component that they fitted to the interstellar absorption to be different from solar but, unfortunately, they do not report the best fitting values of these parameters. On the other hand, using the Reflection Grating Spectrometer on board *XMM-Newton*, Pinto et al. (2013) measured the abundance of O, Ne, Mg, and Fe in the interstellar medium (ISM) in the direction of nine low-mass X-ray binaries, not including 4U 1630–47. Interestingly, they found that the Fe abundance in the neutral ISM in the direction of these sources ranges between less than 0.02 and 0.50 times the solar abundance. Because the putative lines reported by Díaz Trigo et al. (2013) are close to the K- α edges of (neutral) Ca I (4.04 keV), Fe I (7.12 keV), and Ni I (8.34 keV), and the column density toward 4U 1630–47 is quite high (see above), the results of Pinto et al. (2013) suggest the possibility that the emission lines reported by Díaz Trigo et al. (2013) could in fact be an artefact of the model if the incorrect elemental abundance in the ISM is used in the fits. (Díaz Trigo et al. 2013, assumed solar abundance in their fits.)

In this paper, we used the same *XMM-Newton* data of 4U 1630–47 as Díaz Trigo et al. (2013), but we explore an alternative model in which we allow the abundance of the ISM to be different from solar. We can fit the data well with a model that does not require any Doppler-shifted emission lines; instead, our fits yield non-solar abundances of S and Fe in the ISM along the line of sight to the source. Our model not only fits the two observations in Díaz Trigo et al. (2013), but also the other *XMM-Newton* observations during the 2012 outburst (Díaz Trigo et al. 2014), in which four absorption lines, that we identify as being produced by Fe xxv, Fe xxvi and Ni xxviii (or Fe xxv Ly β), and two absorption K-edges, due to Fe xxv and Fe xxvi, are detected. Furthermore, the putative Doppler-shifted emission lines are not required either using the same model as Díaz Trigo et al. (2013) when we apply the new calibration files to those observations.

2 OBSERVATIONS AND DATA REDUCTION

The X-ray data that we used here consist of six observations of 4U 1630–47 with *XMM-Newton* (Jansen et al. 2001) taken between March 4 and September 28 2012. We report the details of the observations in Table 1. We only used data from the European Photon Imaging Camera, EPIC-pn (Strüder et al. 2001), which was operated in either burst or timing mode. To reduce and analyse the raw data we used version 14.0.0 of the *XMM-Newton* Scientific Analysis Software (SAS) package following standard procedures.

We used the command *epproc* to calibrate the timing- and burst-mode photon event files. Following the recommendations of the *XMM-Newton* team, for the burst-mode data we also ran the command *epfast*. This command applies a correction to the energy scale due to charge transfer inefficiency in the CCD in burst mode. While there is some discussion in the literature regarding the applicability of this correction (see Walton et al. 2012, and the

XMM-Newton Calibration Technical Note of November 2014¹), Díaz Trigo et al. (2013) applied this correction during their analysis and therefore, in order to compare to their results, we apply it here. For completeness, we also reduced the burst-mode observations without applying the *epfast* correction.

We selected calibrated events with PATTERN ≤ 4 in the central CCD of the EPIC-pn camera to get the spectrum of the source and we extracted a background spectrum from the outer columns of the central CCD (see Table 1 for the parameters of the extraction regions).

The difference between timing and burst mode in the process of extracting the data is that the spectra of the latter are influenced by the value of RAWY, i.e., the CCD row number (Kirsch et al. 2006). Following the recommendations of the *XMM-Newton* team, we excluded events with RAWY > 140. We rebinned the average EPIC-pn spectra before fitting in order to have a minimum of 25 counts in each bin. We created the redistribution matrix file (RMF) and the ancillary response file (ARF) using the SAS tasks *rmfgen* and *arfgen*, respectively. Following Díaz Trigo et al. (2013), we fitted the EPIC-pn spectra between 2 and 10 keV.

We used the spectral analysis package XSPEC v12.8.2 to fit the data, adding a 1% systematic error to the model to account for calibration uncertainties. The models that we used in this paper include a component to account for photoelectric absorption of the interstellar material along the line of sight. For this component we used either TBABS or VPHABS; the latter allows variable abundances in the interstellar material. For the emission component we used DISKBB, a multi-colour disc blackbody (Mitsuda et al. 1984), POWERLAW, a simple power law, and GAUSS, to account for possible Gaussian emission lines. We added several Gaussian absorption lines and edges (EDGE), when necessary. Throughout the paper, we give the 1σ errors for all fitted parameters and, when required, the 95% confidence upper limits.

3 RESULTS

To compare our results with those of Díaz Trigo et al. (2013), we first fitted the two burst-mode observations, separately from the timing-mode observations, using the same calibration files that Díaz Trigo et al. (2013) used. We then fitted our model simultaneously to the two burst- and the four timing-mode observations. Finally we fitted the same model only to the burst-mode observations using the latest calibration.

3.1 Fits to the two burst-mode observations using the old calibration files

Following Díaz Trigo et al. (2013), we first used the model TBABS*(DISKBB+POWERLAW+GAUSS₁+GAUSS₂+GAUSS₃) to fit the two burst-mode observations. To reproduce their procedures as close as possible, we allowed N_H to vary between the two observations. Similar to Díaz Trigo et al. (2013), we found three emission lines in ObsID 0670673201, but not in ObsID 0670673101. In the latter case we calculated the upper limit to those lines assuming that they had the same energy and width as the lines in the other observation. We got values of the parameters that, except for N_H and the normalisation of the DISKBB and the GAUSS components, were similar

¹ <http://xmm.vilspa.esa.es/docs/documents/CAL-TN-0083.pdf>

Table 1. XMM-Newton Observations of 4U 1630–47 used in this paper

ObsID	Observation Time (UTC) (day/month/year hh:mm)	Observation mode	RAWX source	RAWX back
0670671501-1	04/03/2012 11:24 - 04/03/2012 12:27	Timing	[27,46]	[4,10]
0670671501-2	04/03/2012 13:43 - 05/03/2012 09:23	Timing	[28,45]	[4,10]
0670671301	20/03/2012 19:54 - 21/03/2012 02:30	Timing	[28,45]	[4,10]
0670672901	25/03/2012 04:14 - 25/03/2012 21:56	Timing	[28,45]	[4,10]
0670673001	09/09/2012 21:14 - 10/09/2012 07:49	Timing	[28,45]	[4,10]
0670673101	11/09/2012 20:56 - 12/09/2012 05:38	Burst	[20,51]	[4,10]
0670673201	28/09/2012 07:16 - 28/09/2012 21:48	Burst	[20,51]	[4,10]

Notes. ObsID 0670671501 contains two separate event files in timing mode that we extracted and fitted separately. We called them 0670671501-1 and 0670671501-2, respectively. RAWX source and RAWX back indicate the extraction region in the CCD for the source and the background, respectively.

Table 2. Best-fitting parameters for the two burst-mode observations of 4U 1630–47 based on the old calibration using two models

		Model of Díaz Trigo et al. (2013)		Our model	
ObsID		0670673101	0670673201	0670673101	0670673201
TBABS/vPHABS	N_H (10^{22} cm $^{-2}$)	8.80 ± 0.05	8.85 ± 0.08	15.0 ± 0.2 ^[1]	15.0 ± 0.2 ^[1]
	S/S $_{\odot}$	1.0^f	1.0^f	1.32 ± 0.06 ^[2]	1.32 ± 0.06 ^[2]
	Fe/Fe $_{\odot}$	1.0^f	1.0^f	0.54 ± 0.07 ^[3]	0.54 ± 0.07 ^[3]
DISKBB	kT_{in} (keV)	1.73 ± 0.01	1.75 ± 0.02	1.67 ± 0.01	1.68 ± 0.02
	k_{dbb}	90.7 ± 2.0	91.9 ± 3.6	107.7 ± 3.0	110.6 ± 3.8
POWERLAW	Γ	2^f	2^f	2^f	2^f
	k_{pow}	< 0.23	1.03 ± 0.14	< 0.44	1.10 ± 0.09
GAUSS1	E (keV)	4.02 ± 0.06 ^[4]	4.02 ± 0.06 ^[4]	$7.0^{+0.0}_{-0.05}$ ^[5]	$7.0^{+0.0}_{-0.05}$ ^[5]
	σ (eV)	165^{+47}_{-53} ^[6]	165^{+47}_{-53} ^[6]	183^{+108}_{-79} ^[7]	183^{+108}_{-79} ^[7]
	k_{gau}	< 2.3	5.8 ± 1.8	< 2.3	1.61 ± 0.6
	W (eV)	< 15.9	13.8 ± 3.6	< 12.2	15.4 ± 6.9
GAUSS2	E (keV)	7.24 ± 0.04 ^[8]	7.24 ± 0.04 ^[8]		
	σ (eV)	165^{+47}_{-53} ^[6]	165^{+47}_{-53} ^[6]		
	k_{gau}	< 0.9	3.0 ± 0.7		
	W (eV)	< 21.7	31.2 ± 6.7		
GAUSS3	E (keV)	8.12 ± 0.10 ^[9]	8.12 ± 0.10 ^[9]		
	σ (eV)	165^{+47}_{-53} ^[6]	165^{+47}_{-53} ^[6]		
	k_{gau}	< 0.5	1.5 ± 0.6		
	W (eV)	< 42.8	$23.7^{+7.5}_{-8.0}$		
χ^2_{ν}		0.98 for 256 d.o.f.		0.86 for 259 d.o.f.	

N_H is the column density of the neutral absorber.

S/S $_{\odot}$ and Fe/Fe $_{\odot}$ are, respectively, the sulphur and iron abundances, in solar units, of the absorber along the line of sight.

k_{dbb} , equal to the cosine of the inclination of the accretion disc with respect to the line of sight times the square of the ratio of the inner radius of the disc in km and the distance to the source in units of 10 kpc, k_{pow} , in units of photons keV $^{-1}$ cm $^{-2}$ s $^{-1}$ at 1 keV, and k_{gau} , in units of 10^{-3} photons cm $^{-2}$ s $^{-1}$, are, respectively, the normalisation of the DISKBB, POWERLAW and GAUSS components.

W is the equivalent width of the line.

Parameters with the same number in between square brackets were linked to be the same during the fit.

^f This parameter was kept fixed at the given value during the fits.

^p The energy of this emission line pegged at the upper limit.

to those in Díaz Trigo et al. (2013). The difference in the normalisations is likely due to the fact that we considered the background spectrum in the analysis, whereas Díaz Trigo et al. (2013) did not. We give the best-fitting parameters for this model in Table 2, and we plot the X-ray spectra and best-fitting model of the two burst-mode observations in Figure 1. As in Díaz Trigo et al. (2013), to highlight the three emission lines we set their normalisations to zero in the residuals plot.

We then fitted an alternative model to the same data, in which we replaced the TBABS component by the vPHABS component, and we kept only one of the GAUSS emission components. The other components were the same as those in the model of Díaz Trigo et al. (2013). In this case we fitted the same model to both spectra si-

multaneously and, since the interstellar absorption along the line of sight to the source should not change, we linked the parameters of vPHABS between the two observations. We changed the default solar abundances model (ABUND in XSPEC) to the abundances of Wilms et al. (2000) and the default photoelectric absorption cross-sections table (XSPEC in XSPEC) to that given by Verner et al. (1996). We fixed the photon index, Γ , of the POWERLAW component at 2, since it could not be well constrained in the fits.

One by one, we let the abundance of C, N, O, Ne, Mg, Si, S, Ca, Fe, and Ni in vPHABS free to fit the data, while the other element abundances were kept fixed at the solar values. Except for the case of S and Fe, the best-fitting abundances were consistent with solar,

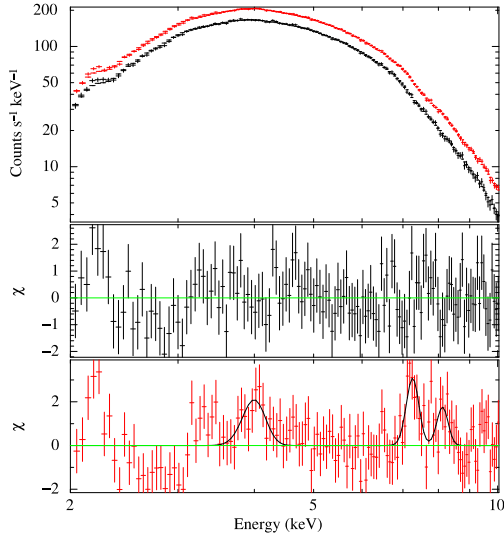


Figure 1. X-ray spectra of ObsID 0670673101 and 0670673201 of 4U 1630–47 fitted with the model of Díaz Trigo et al. (2013). The second panel is the residual of the best-fitting of ObsID 0670673101; the third panel is the residual of ObsID 0670673201 when the strength of the three GAUSS components is set to zero. For this, and the other figures, the residuals are the data minus the model divided by the error.

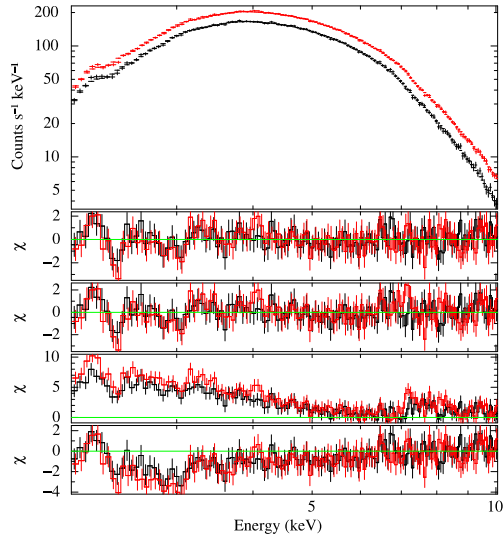


Figure 2. X-ray spectra of ObsIDs 0670673101 and 0670673201 of 4U 1630–47 fitted simultaneously with the alternative model that we proposed here. The second panel shows the residual of the best-fitting model to the two observations; the following panels are the residuals of best-fitting model when the strength of the GAUSS component is set to zero (third panel from the top), the abundance of S in vPHABS is set to solar (fourth panel from the top), and the abundance of Fe in vPHABS is set to solar (bottom panel).

and hence we eventually left the S and Fe abundance free and fixed all the other abundances to solar to fit the data.

Our best-fitting model contains a moderately broad Gaussian line at 7 keV, consistent with the Ly α line of Fe xxvi. A marginal detection of a similar line, likely due to reflection off the accretion disc, had been previously reported in this source (Tomsick & Kaaret 2000; Tomsick et al. 2014). Since Fe reflection lines should appear between 6.4 keV (Fe i) and 6.97 keV (Fe xxvi), we constrained the line to be in the range 6.4 – 7 keV during the

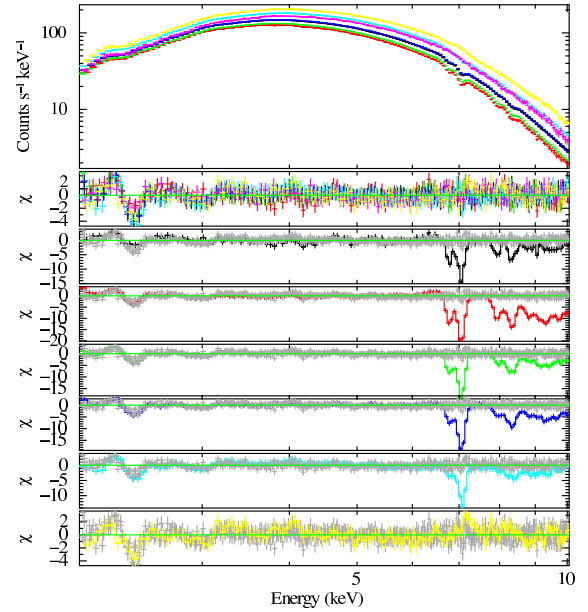


Figure 3. X-ray spectra of all the six *XMM-Newton* observations of 4U 1636–47 fitted simultaneously. The second panel from the top shows the residuals of the best-fitting model to all observations; the following panels are the residuals of each observation when the strength of the emission and absorption components are set to zero. Each color corresponds to one observation in Table 1, in the sequence black, red, green, blue, light blue, magenta and yellow. We do not show a residual panel for ObsID 0670673101 (magenta) because there are no emission or absorption components in this observation.

fits. The best-fitting value of the energy of the line pegged at the upper limit of this range, which could be in partly due to an imperfect calibration of the energy scale in burst-mode. The reduced χ^2 of our model is $\chi^2_{\nu} = 0.86$ for 259 d.o.f. We plot the data and our best-fitting model in Figure 2, and show the best-fitting parameters of these two observations using our model in Table 2. The residual panels in this figure show the effect of the different parameters to the fit. The fit does not require any relativistically Doppler red- or blueshifted emission line. Instead, the abundance of S in vPHABS is higher than solar, 1.32 ± 0.06 , and that of Fe is lower than solar, 0.54 ± 0.07 .

As a final check, we also created calibrated event files without applying the *epfast* correction and fitted the spectra with our model with variable sulphur and iron abundances. Since the best-fitting parameters in this case are consistent, within errors, with those from the fits to the spectra for which we did apply the *epfast* correction, we do not show a plot of this analysis. The only difference between the two sets of spectra is that in the model for the data for which we do not apply *epfast* we need to add an extra, marginally significant, emission line at 6.65 ± 0.09 keV in the model of ObsID 0670673101.

3.2 Fits to the burst- and timing-mode observations using the old calibration

We subsequently fitted our new model to all seven spectra simultaneously. A quick inspection of the residual plots indicated, in some cases, the presence of absorption features at energies of ~ 6.5 keV or higher. Therefore we added up to four Gaussian absorption lines, using negative GAUSS in XSPEC, and two edges, EDGE in XSPEC, to account for possible absorption from highly ionised ma-

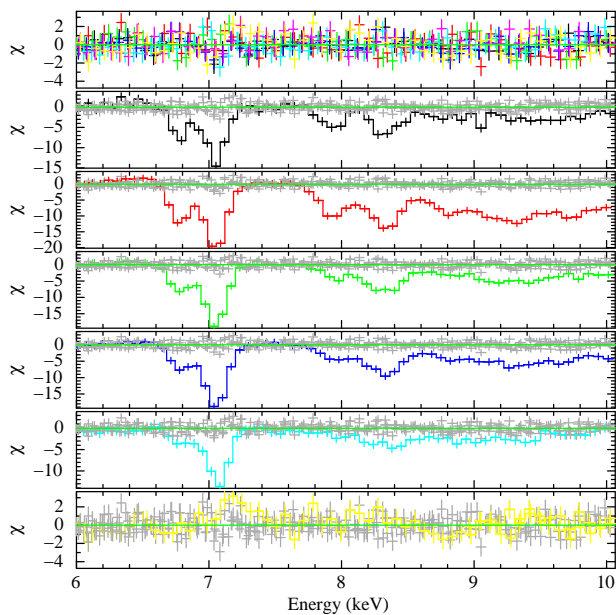


Figure 4. All the residuals of the burst- and timing-mode observations except ObsID 0670673101.

terial close to the source. Not all these components were required in all observations. To keep the model as simple as possible, when the best-fitting parameters of these absorption components turned to be similar within errors, we linked these parameters across the observations. The model we fitted, $\text{vphabs}^*(\text{diskbb} + \text{gauss} + \text{powerlaw} - \text{gauss}_1 - \text{gauss}_2 - \text{gauss}_3 - \text{gauss}_4) * \text{edge}_1 * \text{edge}_2$, gives an acceptable fit, with $\chi^2_\nu = 0.99$ for 895 d.o.f.. We show the best-fitting parameters in Table 3 and plot the spectra and best-fitting model of all the observations in Figure 3. In order to show the emission and absorption lines and edges in each observation, we set the strength of these components to zero in the residual panels (see Figure 3). In Figure 4 we show a zoom in of the residual panels of Figure 3 in the energy range 6–10 keV.

Compared to the parameters in Kubota et al. (2007), Rózańska et al. (2014) and Díaz Trigo et al. (2014), we find a higher value of N_H than theirs and the temperature of the disc is higher than that of Kubota et al. (2007). The energy of the absorption lines and edges are consistent with those of Fe xxv He α (6.70 keV), Fe xxvi Ly α (6.97 keV), Ni xxviii Ly α (8.09 keV) or Fe xxv Ly β (7.88 keV), Fe xxvi Ly β (8.25 keV), Fe xxv K-edge (8.83 keV) and Fe xxvi K-edge (9.28 keV), similar to the identification in Díaz Trigo et al. (2014). However, the results are not identical; e.g., Díaz Trigo et al. (2014) reported an absorption edge at 8.67 keV in ObsID 0670671301 that is not required in our fits. Rózańska et al. (2014) detected seven iron absorption lines with *Suzaku*, four of which are Fe xxv He α , Fe xxvi Ly α , Fe xxv Ly β and Fe xxvi Ly β , the same ones we report here. The remaining two absorption lines identified by Rózańska et al. (2014) are Fe xxv Ly γ and Fe xxvi Ly γ , which we do not detect here.

We plot the equivalent width of the emission and absorption lines as a function of the total unabsorbed flux in the 2–10 keV range in Figure 5. From this figure it appears that the equivalent width of the emission and absorption lines is anti-correlated with the total unabsorbed flux. To test this we fitted both a constant and a linear function to each of these relations to assess whether the decreasing trend is significant. For the case of the absorption lines the F-test probabilities range from 3×10^{-6} to 7×10^{-2} , indicating

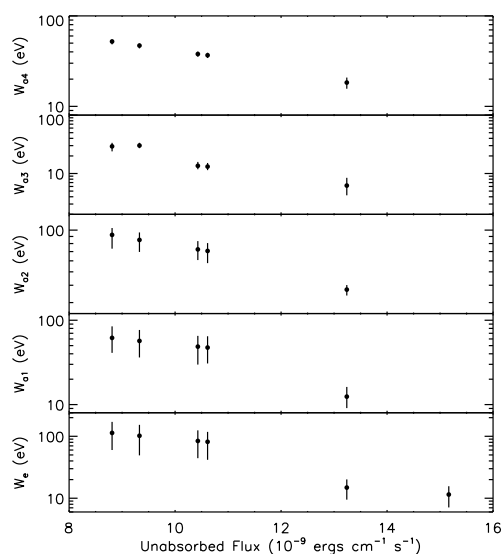


Figure 5. The equivalent width of the broad emission and narrow absorption lines of 4U 1630–47 as a function of the total unabsorbed flux in the 2–10 keV range. W_e and W_{a1} to W_{a4} represent, respectively, the equivalent width of the emission and absorption lines of Fe xxv He α , Fe xxvi Ly α , Ni xxviii Ly α or Fe xxv He β and Fe xxvi Ly β .

that in most cases the decrease of the equivalent width with flux is significant. For the emission line, however, the F-test suggests that a linear function is not significantly better than a constant. Since the emission and absorption lines in this part of the spectrum respond mostly to the high-energy flux, we also examined the plots of the line equivalent widths vs. the 7–10 keV flux; the trends are the same as those in Figure 5 for which we used the 2–10 keV flux, and hence we do not show those plots here.

In Figure 6 we plot some of the fitting parameters as a function of time. In the top panel of Figure 6 we show the MAXI (Monitor of All-sky X-ray Image, Matsuoka et al. 2009) light curve of 4U 1630–47 in the 2–10 keV energy band from MJD 55970 to MJD 56220. The other panels show, respectively, the time histories of the temperature, the normalisation and the flux of the diskbb component, and the flux of the powerlaw component. We do not plot the emission gauss component in this figure because we linked the parameters of this component across several observations (see Table 3). Figure 6 shows that the temperature of the diskbb component generally increases with time, whereas the normalisation shows the opposite trend; on average, the flux of the diskbb and powerlaw components appear to increase with time. The temperature of the disc and the disc and power-law fluxes are generally correlated, whereas the disc normalisation is anti-correlated, with the 2–10 keV MAXI flux. This is consistent with the standard scenario of black-hole states, but given the long time gaps between the observations, and the complex changes of the light curve with time (top panel of Figure 6), we do not discuss these correlations further. The powerlaw component in ObsID 0670673101 is not significant, and therefore we plotted the upper limit as a triangle. From this figure it is apparent that the emission in the 2–10 keV range is always dominated by the diskbb component.

Table 3. Parameters of the emission and absorption lines and edges in the *XMM-Newton* observations of 4U 1630–47.

ObsID	0670671501-1	0670671501-2	0670671301	0670672901	0670673001	0670673101	0670673201
$a N_{\mathrm{H}}$ (10^{22} cm $^{-2}$)	14.1 \pm 0.1 ^[1]	14.1 \pm 0.1 ^[1]	14.1 \pm 0.1 ^[1]	14.1 \pm 0.1 ^[1]	14.1 \pm 0.1 ^[1]	14.1 \pm 0.1 ^[1]	14.1 \pm 0.1 ^[1]
$b S/S_{\odot}$	1.47 \pm 0.02 ^[2]	1.47 \pm 0.02 ^[2]	1.47 \pm 0.02 ^[2]	1.47 \pm 0.02 ^[2]	1.47 \pm 0.02 ^[2]	1.47 \pm 0.02 ^[2]	1.47 \pm 0.02 ^[2]
$b \mathrm{Fe}/\mathrm{Fe}_{\odot}$	0.95 \pm 0.04 ^[3]	0.95 \pm 0.04 ^[3]	0.95 \pm 0.04 ^[3]	0.95 \pm 0.04 ^[3]	0.95 \pm 0.04 ^[3]	0.95 \pm 0.04 ^[3]	0.95 \pm 0.04 ^[3]
GAUSS _e	E (keV)	6.89 \pm 0.02 ^[4]	6.89 \pm 0.02 ^[4]	6.89 \pm 0.02 ^[4]	6.89 \pm 0.02 ^[4]	6.89 \pm 0.02 ^[4]	6.89 \pm 0.02 ^[4]
	σ (eV)	169.1 $^{+13.5}_{-23.1}$ ^[5]	169.1 $^{+13.5}_{-23.1}$ ^[5]	169.1 $^{+13.5}_{-23.1}$ ^[5]	169.1 $^{+13.5}_{-23.1}$ ^[5]	169.1 $^{+13.5}_{-23.1}$ ^[5]	169.1 $^{+13.5}_{-23.1}$ ^[5]
	k_{gau}	4.6 $^{+1.0}_{-0.5}$ ^[6]	4.6 $^{+1.0}_{-0.5}$ ^[6]	4.6 $^{+1.0}_{-0.5}$ ^[6]	4.6 $^{+1.0}_{-0.5}$ ^[6]	1.3 \pm 0.5 ^[7]	1.3 \pm 0.5 ^[7]
	W (eV)	113.4 $^{+57.5}_{-53.4}$	102.0 $^{+51.1}_{-52.8}$	84.1 $^{+40.6}_{-39.8}$	81.6 $^{+36.4}_{-39.8}$	14.9 \pm 5.4	< 12.4
GAUSS _{a1}	E (keV)	6.78 \pm 0.01 ^[8]	6.78 \pm 0.01 ^[8]	6.78 \pm 0.01 ^[8]	6.78 \pm 0.01 ^[8]	6.78 \pm 0.01 ^[8]	6.78 \pm 0.01 ^[8]
	σ (eV)	10.0 $^{+12.2}_{-10.0P}$ ^[9]	10.0 $^{+12.2}_{-10.0P}$ ^[9]	10.0 $^{+12.2}_{-10.0P}$ ^[9]	10.0 $^{+12.2}_{-10.0P}$ ^[9]	10.0 $^{+12.2}_{-10.0P}$ ^[9]	10.0 $^{+12.2}_{-10.0P}$ ^[9]
	k_{gau}	3.4 \pm 0.5 ^[10]	3.4 \pm 0.5 ^[10]	3.4 \pm 0.5 ^[10]	3.4 \pm 0.5 ^[10]	1.2 \pm 0.3	< 1.1
	W (eV)	65.5 $^{+25.9}_{-24.2}$	60.3 $^{+23.2}_{-19.0}$	51.7 $^{+18.5}_{-17.6}$	50.4 $^{+18.9}_{-17.5}$	21.2 \pm 7.2	< 20.9
GAUSS _{a2}	E (keV)	7.03 \pm 0.01 ^[11]	7.03 \pm 0.01 ^[11]	7.03 \pm 0.01 ^[11]	7.03 \pm 0.01 ^[11]	7.03 \pm 0.01 ^[11]	7.03 \pm 0.01 ^[11]
	σ (eV)	10.0 $^{+4.3}_{-10.0P}$ ^[12]	10.0 $^{+4.3}_{-10.0P}$ ^[12]	10.0 $^{+4.3}_{-10.0P}$ ^[12]	10.0 $^{+4.3}_{-10.0P}$ ^[12]	10.0 $^{+4.3}_{-10.0P}$ ^[12]	10.0 $^{+4.3}_{-10.0P}$ ^[12]
	k_{gau}	4.4 \pm 0.6 ^[13]	4.4 \pm 0.6 ^[13]	4.4 \pm 0.6 ^[13]	4.4 \pm 0.6 ^[13]	3.1 \pm 0.3	< 0.5
	W (eV)	95.2 $^{+17.4}_{-9.5}$	87.5 $^{+13.9}_{-10.7}$	74.9 $^{+14.6}_{-8.9}$	73.0 $^{+12.5}_{-9.9}$	45.2 $^{+4.4}_{-3.3}$	< 12.0
GAUSS _{a3}	E (keV)	7.93 \pm 0.01 ^[14]	7.93 \pm 0.01 ^[14]	7.93 \pm 0.01 ^[14]	7.93 \pm 0.01 ^[14]	7.93 \pm 0.01 ^[14]	7.93 \pm 0.01 ^[14]
	σ (eV)	10.0 $^{+27.6}_{-10.0P}$ ^[15]	10.0 $^{+27.6}_{-10.0P}$ ^[15]	10.0 $^{+27.6}_{-10.0P}$ ^[15]	10.0 $^{+27.6}_{-10.0P}$ ^[15]	10.0 $^{+27.6}_{-10.0P}$ ^[15]	10.0 $^{+27.6}_{-10.0P}$ ^[15]
	k_{gau}	0.5 \pm 0.06 ^[16]	0.8 \pm 0.1	1.0 \pm 0.07	0.5 \pm 0.06 ^[16]	0.3 \pm 0.1	< 0.2
	W (eV)	29.2 \pm 4.5	30.2 $^{+2.7}_{-3.2}$	13.6 \pm 2.1	13.2 \pm 2.1	6.0 $^{+2.5}_{-2.1}$	< 249.0
GAUSS _{a4}	E (keV)	8.32 \pm 0.01 ^[17]	8.32 \pm 0.01 ^[17]	8.32 \pm 0.01 ^[17]	8.32 \pm 0.01 ^[17]	8.32 \pm 0.01 ^[17]	8.32 \pm 0.01 ^[17]
	σ (eV)	67.6 $^{+15.2}_{-12.7}$ ^[18]	67.6 $^{+15.2}_{-12.7}$ ^[18]	67.6 $^{+15.2}_{-12.7}$ ^[18]	67.6 $^{+15.2}_{-12.7}$ ^[18]	67.6 $^{+15.2}_{-12.7}$ ^[18]	67.6 $^{+15.2}_{-12.7}$ ^[18]
	k_{gau}	1.2 \pm 0.1 ^[19]	1.2 \pm 0.1 ^[19]	1.2 \pm 0.1 ^[19]	1.2 \pm 0.1 ^[19]	0.8 \pm 0.1	< 0.5
	W (eV)	52.3 $^{+3.5}_{-2.4}$	47.1 $^{+3.3}_{-2.3}$	38.0 \pm 2.4	36.9 \pm 2.4	18.1 \pm 2.4	< 287.6
EDGE ₁	E (keV)	8.63 \pm 0.02 ^[20]	8.63 \pm 0.02 ^[20]	8.63 \pm 0.02 ^[20]	8.63 \pm 0.02 ^[20]	8.63 \pm 0.02 ^[20]	8.63 \pm 0.02 ^[20]
	τ	0.12 \pm 0.01 ^[21]	0.12 \pm 0.01 ^[21]	0.04 \pm 0.01 ^[21]	0.04 \pm 0.01 ^[21]	0.04 \pm 0.01 ^[21]	< 0.03
EDGE ₂	E (keV)	9.05 \pm 0.04 ^[22]	9.05 \pm 0.04 ^[22]	9.05 \pm 0.04 ^[22]	9.05 \pm 0.04 ^[22]	9.05 \pm 0.04 ^[22]	9.05 \pm 0.04 ^[22]
	τ	< 0.04	0.04 \pm 0.01 ^[23]	0.04 \pm 0.01 ^[23]	0.04 \pm 0.01 ^[23]	< 0.004	< 0.02
χ^2_{ν}	0.99 for 895 d.o.f.						

Notes. The GAUSS_e and GAUSS_{a1} to GAUSS_{a4} components represent the emission and absorption lines of Fe xxv He α , Fe xxvi Ly α , Ni xxvii Ly α or Fe xxv He β and Fe xxvi Ly β , respectively.

The EDGE₁ and EDGE₂ components indicate the absorption K-edges of Fe xxv and Fe xxvi, respectively.

See Table 2 for the definition and units of the parameters. The symbols used in this Table have the same meaning as in Table 2. As in Table 2, superscripts indicate parameters that were linked between observations during the fits.

3.3 Fits to two burst-mode observations using the new calibration

While we were analysing these data, the *XMM-Newton* team released a new set of calibration files (dated March 31 2015) for Epic-pn burst-mode observations. We therefore extracted the burst-mode spectra again using the new calibration, and fitted our model to these two observations of 4U 1630–47. Comparing to the previous fitting results of the two burst-mode observations using the old calibration, we added an extra negative GAUSS component to the model to account for a possible absorption line at ~ 7 keV. We list our best-fitting parameters in Table 4. The F-test probabilities for the emission and absorption lines are, respectively, 10^{-2} and 10^{-3} , indicating that the lines are marginally significantly. We also tried to fit these data using the model of Díaz Trigo et al. (2013), but the three emission lines are not significantly detected. Finally, we also reduced these two burst-mode observations using the new calibration without applying the *epfast* correction. The best-fitting parameters are consistent, within errors, with those from the other fits, and in this case we do not find any significant emission line in ObsID 0670673201 either.

4 DISCUSSION

Recently, Díaz Trigo et al. (2013) reported the detection of three Doppler-shifted emission lines arising from the jet of 4U 1630–47

Table 4. Best-fitting parameters for the two burst-mode observations of 4U 1630–47 based on the new calibration files using our model.

ObsID	0670673101	0670673201
TBABS/VHFPABS	N_{H} (10^{22} cm $^{-2}$)	13.8 \pm 0.2 ^[1]
	S/S_{\odot}	1.28 \pm 0.06 ^[2]
	$\mathrm{Fe}/\mathrm{Fe}_{\odot}$	0.74 \pm 0.08 ^[3]
DISKBB	Tin (keV)	1.65 \pm 0.02
	k_{dbb}	115.2 \pm 3.9
POWERLAW	Γ	2 f
	k_{pow}	0.26 \pm 0.09
GAUSS _e	E (keV)	6.58 $^{+0.38}_{-0.09}$ ^[4]
	σ (eV)	135.7 $^{+181.3}_{-74.6}$ ^[5]
	k_{gau}	1.4 $^{+92.1}_{-0.5}$
	W (eV)	13.9 $^{+15}_{-13.9}$
GAUSS _a	E (keV)	6.99 $^{+0.06}_{-6.99P}$ ^[6]
	σ (eV)	87 $^{+159}_{-86.4}$ ^[7]
	k_{gau}	1.3 $^{+0.5}_{-20.4}$
	W (eV)	16.2 $^{+11.2}_{-15.6}$
χ^2_{ν}	0.74 for 256 d.o.f.	

Notes. See Table 2 for the definition and units of the parameters. The symbols used in this Table have the same meaning as in Tables 2 and 3. Also, as in Table 2, superscripts indicate parameters that were linked between observations during the fits.

in an *XMM-Newton* observation obtained during the 2012 outburst of the source. Here we show that this same observation can be well fitted with a model that does not require the three

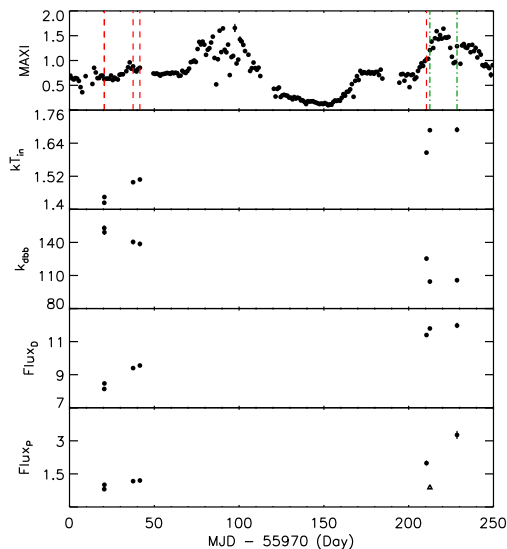


Figure 6. Light curve and time history of some fitting parameters of 4U 1630–47. The upper panel shows the MAXI light curve (in units of photons $\text{cm}^{-2}\text{s}^{-1}$) in the 2–10 keV band. The green dashed-dotted and red dashed vertical lines indicate the times of the two burst-mode and the four timing-mode *XMM-Newton* observations, respectively. The second and third panels show, respectively, the temperature (in units of keV) and normalisation of the *DISKBB* component. The fourth and fifth panels show the 2–10 keV unabsorbed flux, in units of $10^{-9} \text{ erg cm}^{-2} \text{ s}^{-1}$, of the *DISKBB* and *POWERLAW* components, respectively. The triangle in the fifth panel denotes the 95% confidence upper limit of the flux of the *POWERLAW* component in that observation. Some of the error bars are too small to show up on this plot.

emission lines. The main difference between our model and that of Díaz Trigo et al. (2013) is that we allow the abundance of S and Fe in the interstellar material along the line of sight to the source to vary. Our model also fits well the other observation in Díaz Trigo et al. (2013), in which they do not detect the emission lines. Fitting these two observations simultaneously, we find that the abundances of S and Fe in the interstellar medium toward the source are, respectively, 1.32 ± 0.06 and 0.54 ± 0.07 , in solar units. Because of the large value of the column density in the interstellar medium toward the source, a non-solar abundance of these elements impacts upon the model at energies around the neutral Fe edge, at ~ 7.1 keV (see the two bottom panels in Figure 2), such that the emission lines are no longer required in the model. Our model also fits the rest of the *XMM-Newton* observation of the 2012 outburst of 4U 1630–47 (Díaz Trigo et al. 2014); in this case, similar to Díaz Trigo et al. (2014), we need to add several absorption lines and edges in the 6.7–9.1 keV energy range, likely due to photo-ionised material close to the source.

Since the two models are fundamentally different, we cannot compare them from a statistical point of view (e.g., using the F-test); however, our model fits the same data with less free parameters, and it is therefore simpler than the one of Díaz Trigo et al. (2013). Our model does include a moderately broad ($\sigma = 183^{+108}_{-79}$ eV) emission line at 7 keV. This line is consistent with a marginally significant line detected from this (Tomsick & Kaaret 2000; Tomsick et al. 2014; King et al. 2014) and other sources (e.g. Miller 2007), which is usually interpreted as due to emission from the hard (power-law) component reflected off the accretion disc, with the broadening being due to relativistic effects close to the black hole (e.g. Fabian et al. 2012). The fact

that in our fits the best-fitting energy of this line pegs at the upper limit, 7 keV, that we imposed in the model may be partly due to the uncertainties in the energy calibration of the *Epic-pn* burst mode (see below), or to inaccuracies in the cross section tables in the component that we used to fit the interstellar absorption.

Our model yields non-solar abundances of S and Fe in the ISM toward 4U 1630–47. In the case of Fe, our best-fitting abundance is consistent with measurements of the Fe abundance in the ISM toward nine low-mass X-ray binaries (not including 4U 1630–47) using high-resolution spectra from the Reflection Grating Spectrometer on board *XMM-Newton* (Pinto et al. 2013, these authors did not measure the S abundance). This makes our model plausible and, if correct, this could explain why the jet lines were not observed with other satellites (Hori et al. 2014; Neilsen et al. 2014).

While we were analysing these data, the *XMM-Newton* team released a new set of calibration files for the *Epic-pn* burst-mode observations. Using this new calibration, we do not detect the lines reported by Díaz Trigo et al. (2013) either, not even if, as they did, we assume solar abundances for all elements in the ISM (see 3.3). In this case the sulphur and iron abundances, respectively $\text{S}/\text{S}_{\odot} = 1.28 \pm 0.06$ and $\text{Fe}/\text{Fe}_{\odot} = 0.74 \pm 0.08$, are consistent within errors with the ones that we obtained using the old calibration files. Assuming that the new calibration is better than the previous one, this result casts doubt on the presence of the Doppler-shifted lines in this source and, at the same time, it provides a rough estimate of the relative accuracy of the calibration of the *Epic-pn* burst-mode data used by Díaz Trigo et al. (2013).

The model that we propose here provides also a good fit to all six *XMM-Newton* observations of this source during the 2012 outburst. Similar to Díaz Trigo et al. (2014), we find a number of absorption lines and edges in the spectra of the four *XMM-Newton* observations that were obtained using the *EPIC-pn* camera in timing mode. These lines and edges are consistent with being due to Fe xxv, Fe xxvi and Ni xxviii, indicating the existence of highly ionised material in the vicinity of the source. When we fit all observations simultaneously, our model yields a significantly higher Fe abundance, 0.95 ± 0.04 , than in the case when we fit only the two burst-mode observations (the S abundance is consistent with the one we obtained from the two burst-mode observations). This could be due to the fact that we used individual Gaussian lines and edges, instead of a self-consistent model of a warm absorber (see, e.g., Díaz Trigo et al. 2014), to fit the absorption by this highly ionised material. In order to keep our model as simple as possible, we linked the parameters of the absorption lines and edges across the different observations whenever possible. This prevents us from carrying out a detailed analysis of the absorption features in the observations separately. We note, however, that a recent study of 4U 1630–47 with high spectral resolution data from *Chandra* (Miller et al. 2015), showed evidence of at least two separate absorption zones in the disc wind component in this source. Since it is not the purpose of this paper to discuss the disc wind in this source in detail (this aspect of the *XMM-Newton* data presented here was already discussed by Díaz Trigo et al. (2014)), we did not explore this possibility further.

Finally, we find that the equivalent width of the emission and absorption lines is anti-correlated with the 2–10 keV unabsorbed flux. For the absorption lines, the change of the equivalent width with flux is probably due to changes in the ionisation fraction of the ionised material. For the emission line, the drop of the equivalent width could be interpreted as either a change of the ionisation fraction (García et al. 2013), or the effect of light bending close to the black hole (Miniutti & Fabian 2004). If the ionised material that

produces the absorption lines and edges is part of the accretion disc (e.g., the disc atmosphere, [Róžańska et al. 2014](#)), this same material would be the one that produces the reflection component and hence the moderately broad Fe emission line. In that case a single mechanism, a change in the ionisation fraction of the disc, would be responsible for the drop of the equivalent width of both the absorption and emission lines as the flux increases.

ACKNOWLEDGEMENTS

This work has made use of data from the High Energy Astrophysics Science Archive Research Center (HEASARC), provided by NASA/Goddard Space Flight Center (GSFC). This work is partly supported by China Scholarship Council (CSC), under the grant number 201404910530. We thank an anonymous referee for his/her constructive comments that helped us improve this paper.

REFERENCES

- Abe Y., Fukazawa Y., Kubota A., Kasama D., Makishima K., 2005, [PASJ](#), **57**, 629
- Augusteijn T., Kuulkers E., van Kerkwijk M. H., 2001, [A&A](#), **375**, 447
- Barret D., McClintock J. E., Grindlay J. E., 1996, [ApJ](#), **473**, 963
- Díaz Trigo M., Miller-Jones J. C. A., Migliari S., Broderick J. W., Tzioumis T., 2013, [Nature](#), **504**, 260
- Díaz Trigo M., Migliari S., Miller-Jones J. C. A., Guainazzi M., 2014, [A&A](#), **571**, A76
- Fabian A. C., et al., 2012, [MNRAS](#), **424**, 217
- García J., Dauser T., Reynolds C. S., Kallman T. R., McClintock J. E., Wilms J., Eikmann W., 2013, [ApJ](#), **768**, 146
- Hjellming R. M., et al., 1999, [ApJ](#), **514**, 383
- Hori T., et al., 2014, [ApJ](#), **790**, 20
- Jansen F., et al., 2001, [A&A](#), **365**, L1
- Jones C., Forman W., Tananbaum H., Turner M. J. L., 1976, [ApJ](#), **210**, L9
- King A. L., et al., 2014, [ApJ](#), **784**, L2
- Kirsch M. G. F., et al., 2006, [A&A](#), **453**, 173
- Kubota A., et al., 2007, [PASJ](#), **59**, 185
- Matsuoka M., et al., 2009, [PASJ](#), **61**, 999
- Miller J. M., 2007, [ARA&A](#), **45**, 441
- Miller J. M., Fabian A. C., Kaastra J., Kallman T., King A. L., Proga D., Raymond J., Reynolds C. S., 2015, preprint, ([arXiv:1510.01177](#))
- Miniutti G., Fabian A. C., 2004, [MNRAS](#), **349**, 1435
- Mitsuda K., et al., 1984, [PASJ](#), **36**, 741
- Neilsen J., Coriat M., Fender R., Lee J. C., Ponti G., Tzioumis A. K., Edwards P. G., Broderick J. W., 2014, [ApJ](#), **784**, L5
- Parmar A. N., Stella L., White N. E., 1986, [ApJ](#), **304**, 664
- Parmar A. N., Angelini L., White N. E., 1995, [ApJ](#), **452**, L129
- Pinto C., Kaastra J. S., Costantini E., de Vries C., 2013, [A&A](#), **551**, A25
- Róžańska A., Madej J., Bagińska P., Hryniewicz K., Handzik B., 2014, [A&A](#), **562**, A81
- Strüder L., et al., 2001, [A&A](#), **365**, L18
- Tomsick J. A., Kaaret P., 2000, [ApJ](#), **537**, 448
- Tomsick J. A., Lapshov I., Kaaret P., 1998, [ApJ](#), **494**, 747
- Tomsick J. A., Yamaoka K., Corbel S., Kalemci E., Migliari S., Kaaret P., 2014, [ApJ](#), **791**, 70
- Verner D. A., Ferland G. J., Korista K. T., Yakovlev D. G., 1996, [ApJ](#), **465**, 487
- Walton D. J., Reis R. C., Cackett E. M., Fabian A. C., Miller J. M., 2012, [MNRAS](#), **422**, 2510
- Wilms J., Allen A., McCray R., 2000, [ApJ](#), **542**, 914